Clim. Past Discuss., https://doi.org/10.5194/cp-2017-135
Manuscript under review for journal Clim. Past
Discussion started: 25 October 2017

Climate of the Past Discussions

A comparison of two astronomical tuning approaches for the Oligocene-Miocene Transition from Pacific Ocean Site U1334 and implications for the carbon cycle

Helen M. Beddow[1], Diederik Liebrand[2,*], Douglas S. Wilson[3], Frits J. Hilgen[1], Appy Sluijs[1], Bridget S. Wade[4], Lucas J. Lourens[1]

[1]*Department of Earth Sciences, Faculty of Geosciences, Utrecht University, Heidelberglaan 2, 3584 CS Utrecht, The Netherlands*
[2]*PalaeoClimate.Science, 3501 AB, Utrecht (province), The Netherlands*
[3]*Department of Earth Science University of California, Santa Barbara, CA 93106-9630, United States*
[4]*Department of Earth Sciences, Faculty of Mathematical and Physical Sciences, University College London, Gower Street, London, WC1E 6BT, United Kingdom*
[*]Corresponding author: diederik@palaeoclimate.science

Abstract

Astronomical tuning of sediment sequences requires both unambiguous cycle-pattern recognition in climate proxy records and astronomical solutions, and independent information about the phase relationship between these two. Here we present two astronomically tuned age models for the Oligocene-Miocene Transition (OMT) from Integrated Ocean Drilling Program Site U1334 (equatorial Pacific Ocean) to assess the effect tuning approaches have on astronomically calibrated ages and the geologic time scale. These age models are based on different phase-assumptions between climate proxy records and eccentricity: the first age model is based on an inverse and in-phase assumption of CaCO3 weight (wt%) to Earth's orbital eccentricity, the second age model is based on an inverse and in-phase assumption of benthic foraminifer stable carbon isotope ratios (δ13C) to eccentricity. The phase-assumptions that underpin these age models represent two end-members on the range of possible tuning options. To independently test which tuned age model and tuning

assumptions are correct, we assign their ages to magnetostratigraphic reversals identified in anomaly profiles. Subsequently we compute tectonic plate-pair spreading rates based on the tuned ages. These alternative spreading rate histories indicate that the CaCO3 tuned age model is most consistent with a conservative assumption of constant spreading rates. The CaCO3 tuned age model thus provides robust ages and durations for polarity chrons C6Bn.1n–C6Cn.1r, which are not based on astronomical tuning in the latest iteration of the Geologic Time Scale. Furthermore, it provides independent evidence that the relatively large (several 10,000 years) time lags documented in the benthic foraminiferal isotope records relative to orbital eccentricity, constitute a real feature of the Oligocene-Miocene climate system and carbon cycle. The age constraints from Site U1334 thus provide independent evidence that the delayed responses of the Oligocene-Miocene climate-cryosphere system and carbon cycle resulted from increased nonlinear feedbacks to astronomical forcing.

Keywords

Astronomical tuning, marine carbon cycle, Oligocene Miocene Transition, IODP Site U1334, equatorial Pacific Ocean, geologic time scale

1. Introduction

Astronomically tuned age models are important in studies of Cenozoic climate change, because they shed light on cause and effect relationships between insolation forcing and the linear and nonlinear responses of Earth's climate system (e.g., [*Hilgen et al*., 2012, *Vandenberghe et al.*, 2012; *Westerhold et al.,* submitted]). As more Cenozoic paleoclimate records are generated that use astronomical tuning as the main high-precision dating tool, it is important to understand the assumptions and limitations inherent in this age-calibration method, in particular with respect to assumptions related to phase-relationships between tuning signal and target curves. These phase assumptions have implications for (*i*) determining the absolute timing of events, (*ii*) the understanding of leads and lags in the climate system, and (*iii*) the exact astronomical frequencies that are present in climate proxy records after tuning.

Clim. Past Discuss., https://doi.org/10.5194/cp-2017-135
Manuscript under review for journal Clim. Past
Discussion started: 25 October 2017

Previously published astronomically tuned age-models for high-resolution climate records that span the Oligocene-Miocene Transition (OMT, ~23 Ma), have used different tuning signal curves for sites from different paleoceanographic settings. In addition, different tuning target curves have been applied. For example, records from Sites 926 and 929 from the Ceara Rise (equatorial Atlantic) were tuned using magnetic susceptibility and/or color reflectance records (i.e., proxies for bulk sediment carbonate content) as tuning signal curve, and used obliquity as the main tuning target curve, sometimes with weaker precession and eccentricity components added (e.g. [*Pälike et al.*, 2006a; *Shackleton et al.*, 1999, 2000; *Zachos et al.*, 2001]). In contrast, sediments from Site 1090 from the Agulhas Ridge (Atlantic sector of the Southern Ocean) and Site 1218 from the equatorial Pacific Ocean were tuned using benthic foraminiferal stable oxygen ($\delta^{18}O$) and/or carbon ($\delta^{13}C$) isotope records as tuning signal (e.g. [*Billups et al.*, 2004; *Pälike et al.*, 2006b]). These records used different combinations of eccentricity, obliquity and/or precession as tuning targets (ETP curves).

More recently, Oligocene-Miocene records from Ocean Drilling Program (ODP) Site 1264 and Middle Miocene records from Integrated Ocean Drilling Program (IODP) Site U1335 used the Earth's eccentricity solution as the sole tuning target [*Laskar et al.*, 2004], and lithological data, such as elemental estimates based on X-ray fluorescence (XRF) core scanning records, was used as the sole tuning signal [*Liebrand et al.*, 2016, *Kochhann et al.*, 2016]. The records from both these sites are characterized by a very clear expression of eccentricity, either resulting from productivity dominated cycles (at Site 1264) or dissolution dominated cycles (at Site U1335). The phase relationships between the ~110-ky cycles and 405-ky cycles (in case of Site U1335), in lithologic records and eccentricity, were straightforward to derive [*Liebrand et al*, 2016, *Kochhann et al.*, 2016] and were in agreement with those previously derived using benthic foraminiferal $\delta^{18}O$ and $\delta^{13}C$ records (e.g., *Zachos et al*, 2001, *Pälike et al*, 2006b). An additional advantage of tuning solely to eccentricity is that no phase-assumption to either northern or southern hemisphere precession forcing is needed, and variations in the long-term stability of precession and obliquity due to tidal dissipation and dynamical ellipticity do not affect the astronomically tuned ages.

The different approaches to astronomical age calibration of the Oligocene-Miocene time interval has resulted in large variations in the resulting phase-estimates after tuning between ~110-ky and 405-ky cycles present in both the eccentricity solution and in lithologic and climatologic proxy records. To obtain better constraints for the true phase-relationships of the ~110-ky and 405-ky cycles between benthic foraminiferal stable isotope records and orbital eccentricity, and to better understand the implications that initial phase-assumptions for astronomical age calibration have on absolute ages across the OMT, we need independent dates that are free from tuning phase-assumptions. Previous studies have successfully used plate-pair spreading rates to independently date magnetochron reversals and used these ages as independent age control (e.g., *Hilgen et al*., 1991, *Lourens et al*., 2004).

Here, we present two astronomically tuned age models for previously published high-resolution benthic foraminiferal $\delta^{18}O$ and $\delta^{13}C$ records across the OMT from IODP Site U1334 (eastern equatorial Pacific Ocean) [*Beddow et al.,* 2016]. We select (estimates of) sediment $CaCO_3$ content and benthic $\delta^{13}C$ as tuning signals, because these data represent two end-members in terms of tuning phase assumptions [*Pälike et al*., 2006, *Liebrand et al*., 2016]. We evaluate the ramifications of these different tuning methods for (*i*) absolute ages of magnetochron reversals, and (*ii*) the lead and lags between eccentricity and lithologic/paleoclimate records, by evaluating the spreading rate histories of a suite of tectonic plate-pairs after assigning the tuned ages to the magnetostratigraphic reversals in their anomaly profiles. The constraints given by the long-term evolutions of these potential spreading-rate histories are sufficiently precise to discriminate between tuning options and phase assumptions.

2. Materials and Methods

2.1 Site description

Site U1334, located in the eastern equatorial Pacific (4794 meters below sea level (mbsl), 7°59.998′N, 131°58.408′W), was recovered during IODP Expedition 320 (Fig.1). Upper Oligocene and lower Miocene sediments from Site U1334 were deposited at a paleodepth of ~4200 mbsl and consist of foraminifer- and radiolaria-bearing nannofossil ooze and chalk [*Pälike et al*., 2010, 2012]. An expanded Oligocene-Miocene section with a well-defined magnetostratigraphy was recovered [*Pälike et al*., 2010; *Channell et al*., 2013] (Fig. 2), and a continuous spliced record of Holes A, B and C was placed on a core composite depth scale below seafloor (CCSF-A, equivalent to meters composite depth; Fig. 2) [*Westerhold et al*., 2012a]. Samples were taken along the splice and all results presented here follow this depth model [*Beddow et al*., 2016].

2.2 Coulometric $CaCO_3$ and magnetic susceptibility

To obtain a continuous lithological proxy record, we estimate $CaCO_3$ wt% (hereafter: $CaCO_3$ content), by calibrating high-resolution shipboard magnetic susceptibility data (MS) to lower resolution discrete shipboard coulometric $CaCO_3$ measurements for Site U1334 [*Pälike et al.*, 2010]. Minimum MS (SI unit) values correspond to maximum $CaCO_3$ values. The correlation between coulometric $CaCO_3$ measurements and MS (SI unit) was calculated using a third order polynomial fit, with an r^2 value of 0.79 (Fig. 2), indicating that approximately 80% of the variability in the MS record is caused by changes in the bulk sediment $CaCO_3$ content. Middle Miocene $CaCO_3$ records from nearby Site U1335 show negatively skewed cycle shapes and have been interpreted as a dissolution-dominated signal [*Herbert*, 1994, *Kochhann et al*., 2016]. In contrast, cycle shapes in the $CaCO_3$ content record for the Oligocene-Miocene of Site U1334 are less skewed, suggesting that here $CaCO_3$ content was predominantly controlled by a combination of productivity and dissolution.

2.3 Benthic stable isotope records and magnetostratigraphic age model

We use the benthic foraminifer $\delta^{18}O$ and $\delta^{13}C$ records of Site U1334, which were measured on the *Oridorsalis umbonatus* and *Cibicidoides mundulus* benthic foraminifer species [*Beddow et al*., 2016]. To construct this mixed-species record, *O. umbonatus* values were corrected to *C. mundulus* values based on ordinary least squares linear regression that was based on a the analysis of 180 pairs of for inter-species isotope value comparison was applied and n [*Beddow et al*., 2016]. The benthic stable isotope datasets at Site U1334 were placed on a magnetostratigraphic age model calculated by fitting a third-order polynomial through 14

Clim. Past Discuss., https://doi.org/10.5194/cp-2017-135
Manuscript under review for journal Clim. Past
Discussion started: 25 October 2017

magnetostratigraphic age-depth tie-points (Table 1 and Fig. 4). This magnetostratigraphic age model yields an initial duration of ~21.9 to 24.1 Ma for the study interval (Fig. 3) [*Channell et al*., 2013; *Beddow et al.,* 2016].

2.4 Spectral analysis

We use AnalySeries [*Paillard et al*., 1996] to conduct spectral analyses on the benthic foraminiferal $\delta^{13}C$ and $\delta^{18}O$ and the $CaCO_3$ datasets in the depth domain, on the magnetostratigraphic age model [*Beddow et al*., 2016], and on both astronomically tuned age model options presented here. Prior to analysis, the data were re-sampled and trends longer than 6 m, or 600 ky, were removed using a notch-filter (frequency = 0, bandwidth = 0.015). Blackman Tukey spectral analysis was used to identify dominant periodicities present within the data, which subsequently were filtered using a Gaussian filter. We applied cross-spectral analysis to identify coherency and phase relationships between the eccentricity and the $CaCO_3$, $\delta^{18}O$ and $\delta^{13}C$ chronologies. These calculations were performed at 95% significance. Evolutive spectral analyses were computed using MATLAB.

2.5. Reversal ages based on plate-pair spreading rates

Anomaly profiles for tectonic plate pair spreading rates were recorded [*Wilson*, 1993], and applied subsequently for testing astronomical age models (e.g., [*Hilgen et al*., 1991; *Krijgsman et al*., 1999; *Hüsing et al*., 2007]. The plate pairs that we have selected to compute reversal ages for are in order of decreasing spreading rate: Pacific-Nazca, Pacific-Juan de Fuca, Australia-Antarctic, and Pacific-Antarctic. When multiple plate pairs show simultaneous changes in spreading rate with the same ratio, e.g., all are faster by say 15% in a short time interval, this indicates errors in the astronomical timescale. Data for the Pacific-Nazca pair is limited to the northern part of the system, which is well surveyed from studies of the separation of the Cocos plate from the northern Nazca plate during chron C6Bn [*Lonsdale*, 2005; *Barckhausen et al.,* 2008]. Pacific-Juan de Fuca data are from immediately north of the Mendocino fracture zone. Reversal ages based on these spreading rates are also used in previous timescale calibrations [e.g. *Cande and Kent*, 1992] despite the fact that for the Oligocene-Miocene only the Pacific-plate record survives. *Wilson* [1988] interpreted a sudden change of spreading-rate gradient for this pair from south faster

Clim. Past Discuss., https://doi.org/10.5194/cp-2017-135
Manuscript under review for journal Clim. Past
Discussion started: 25 October 2017

Climate of the Past Discussions

prior to C6Cn.2n(o) to north faster after that reversal. The dataset for the Australia-Antarctic pair is similar to that presented by *Cande and Stock* [2004]. It is expanded from that used by *Lourens et al.* [2004] who assigned reversal ages for 18.52–23.03 Ma based on a spreading rate of 69.9 mm/yr for this plate pair. Data for Pacific-Antarctic come primarily from recent surveys near the Menard and Vacquier fracture zones [*Croon et al*., 2008].

3. Results

3.1. Lithologic and paleoclimatic records

The synthetic wt% calcium carbonate record ($CaCO_3$ est. wt%) ranges between 54% and 88%, consistent with the $CaCO_3$ wt% measurements on discrete samples (Figs. 2, 3). Values decrease to below 70% in the upper Oligocene, between 114.9 and 116.2 m CCSF-A (Fig. 3). From 116.2 m to 121.9 m CCSF-A, the $CaCO_3$ est. wt% varies between 61 and 83%. Variability is generally twice as large in the lower Miocene section of the record, between 88.95 and ~102 m CCSF-A, varying by ~40% with several minima in the record dipping below 70%. There is little variability across the OMT between ~102 and ~106 m CCSF-A. The benthic oxygen isotope record captures the large shift towards positive $\delta^{18}O$ values at the Oligocene-Miocene boundary, with peak positive values (2.43‰) occurring at 104.5 CCSF-A (23.03 Ma). After the boundary, both $\delta^{18}O$ and $\delta^{13}C$ values show higher amplitude variability, and a shift towards more positive values [*Beddow et al*., 2016].

3.2. Spectral Analysis in the depth domain

The power spectra of the $CaCO_3$ content record in the depth domain reveal strong spectral peaks at frequencies of 0.2 cycles/m and 0.65 cycles/m (Fig. 3). These frequencies broadly correspond to those found in the benthic $\delta^{18}O$ and $\delta^{13}C$ depth series at 0.15 cycles/m and 0.65 cycles/m [*Beddow et al.*, 2016]. Smaller spectral peaks are present in the $CaCO_3$ content record at 1.83 cycles/m and 2.8 cycles/m (Fig. 3). High-amplitude cycles with low frequencies are present in all datasets with a 1:4 ratio, suggesting a strong influence from eccentricity forcing (i.e. ~110:405 ky cycles). This interpretation of strong eccentricity is supported by the application of the initial magnetostratigraphic age model [*Beddow et al*., 2016].

4. Astronomical tunings of Site U1334

4.1 Initial age model

As a starting point for astronomical tuning we use an initial magnetostratigraphic age model [*Beddow et al*, 2016; *Channel et al.*, 2013], which is based on the chron reversal ages of the 2012 Geologic Time Scale (GTS2012) [*Vandenberghe et al.*, 2012; *Hilgen et al.*, 2012]. On this initial age model, evolutive and power spectra demonstrate that the $CaCO_3$ content and benthic foraminiferal $\delta^{18}O$ and $\delta^{13}C$ records are dominated by ~110 ky and 405 ky eccentricity paced cycles, with short intervals of significant responses at higher frequencies (Fig. 5). To further assess the influence of eccentricity on the records from Site U1334, we filter the ~110-ky and 405-ky cycles of the $CaCO_3$ est. (%) and $\delta^{13}C$ records (Figs. 6a and 7a). In total, we observe just over five 405-ky cycles in both the filtered $CaCO_3$ content and $\delta^{13}C$ records. There is a notable difference in the number of filtered ~110-ky cycles present between these two datasets. We observe twenty-three ~110-ky cycles in the $CaCO_3$ content record, and twenty-one in the $\delta^{13}C$ record. This is not surprising as the exact number is often very sensitive to the width of the band-pass filter. Visual assessment of the number of cycles is not always straightforward, because not every ~110-ky cycle is expressed equally strong in all data records. In the eccentricity solution for the interval approximately between 21.9 and 24.1 Ma, we count five and a half 405-ky cycles and twenty-two ~110-ky cycles. These numbers are largely in agreement with those obtained from visual assessment and Gaussian filtering.

4.2 Astronomical target curve

For our astronomical target curve, we select Earth's orbital eccentricity. Time-series analyses on the $CaCO_3$ content, and the benthic $\delta^{18}O$ and $\delta^{13}C$ records in the depth domain, and on the initial age model, indicate that eccentricity is the dominant cycle and that higher-frequency cycles are intermittently expressed (Fig. 7). Additional reasons to select eccentricity as the sole tuning target for the OMT of Site U1334 are the uncertain phase relationships of the data records to precession, and the unknown evolution of tidal dissipation and dynamical ellipticity before 10 Ma [*Zeeden et al.*, 2014]. These parameters affect the long-term stability of both the precession and obliquity solutions [*Lourens et al.,* 2004*; Husing et al.,* 2007]. We use the most recent nominal eccentricity solution (i.e., La2011_ecc3L) [*Laskar et al.,* 2011a, 2001b; *Westerhold et al*., 2012b] as tuning target, and for the OMT interval this solution is not significantly different from the La2004 eccentricity solution [*Laskar et al.*, 2004], which was used to generate previous astronomically tuned high-resolution age models for this time interval [*Pälike et al.*, 2006a,b].

4.3. Astronomical age calibration of the OMT from Site U1334

To test different phase-assumptions between the data from Site U1334 and eccentricity, we first consider the $CaCO_3$ content record and then the benthic $\delta^{13}C$ record as tuning signals. Both tuning options are underpinned by assumptions of a consistent and linear in-phase relationship between the tuning signal and the target, eccentricity. Previously tuned climate records for the OMT have shown that these two datasets represent end-members with respect to phase assumptions, with $CaCO_3$ content showing no lag or the smallest lag, and $\delta^{18}O$ and $\delta^{13}C$ showing increasingly larger lags to the ~110-ky and 405-ky eccentricity cycles [*Liebrand et al.*, 2016, *Pälike et al.*, 2006a, *Pälike et al.*, 2006b]. By selecting the $CaCO_3$ content record and the benthic $\delta^{13}C$ chronology, we span the full range of tuned ages that different phase-assumptions between eccentricity and proxy data could imply.

4.3.1. Astronomical tuning using the $CaCO_3$ content record

We use the initial magnetostratigraphic age model as a starting point for a more detailed calibration of maxima in $CaCO_3$ content to ~110-ky eccentricity minima. $CaCO_3$ maxima generally correspond to positive $\delta^{18}O$ values (i.e. cooler, glacial periods), which are usually linked to eccentricity minima and are therefore anticorrelated with eccentricity [*Zachos et al.*, 2001; *Pälike et al.*, 2006a; *Pälike et al.*, 2006b]. The $CaCO_3$ content record has 23 clearly delineated ~110 ky maxima, which we match directly to minima in the La2011 eccentricity time series (Fig. 6c). In addition to these well expressed ~110-ky cycles, we take the expression of the 405-ky cycle into account to establish the tuned age model. The data records from Site U1334 span the interval between 21.96 and 24.15 Ma (2.19 My duration) on the $CaCO_3$ tuned age model. Linear sedimentation rates (LRS) vary between 0.9 and 2.2 cm/ky, with relatively higher sedimentation rates across the OMT (Fig. 6). On average this yields a sample resolution of 3.6 ky for the benthic isotope records.

Evolutive analyses of the benthic $\delta^{18}O$ and $\delta^{13}C$ records on the $CaCO_3$ tuned age model indicate that the 405-ky cycle is best expressed. In contrast, the $CaCO_3$ content record on this age model reveals that the ~110-ky cycle has the highest amplitudes.

Despite the overall clear expression of the 405-ky cycle in the $CaCO_3$ evolutive spectrum, this signal is more subdued across the OMT (Fig. 5). Spectral power at the ~110-ky periodicity increases in all three records in the interval following peak glacial conditions associated with the OMT. This cycle is particularly pronounced in the $\delta^{18}O$ record, and we can identify power at both the 125 ky and the 95 ky eccentricity cycles in both the $CaCO_3$ and $\delta^{18}O$ datasets. We note that this could be a direct result from using eccentricity as a tuning target. For $\delta^{13}C$, the evolutive analysis and power spectra indicate that ~110 ky cycle is more strongly expressed at the 125-ky periodicity, compared to the 95-ky component. We find intermittent power present at a periodicity of ~50 ky/cycle, which is either related to the obliquity cycle that is offset towards a slightly longer periodicity, or to the first harmonic of the ~110-ky eccentricity cycle [*King*, 1996]. The ~50-ky cycle is best expressed in the benthic $\delta^{18}O$ record on the $CaCO_3$ tuned age model, where we identify two main intervals with significant power at this periodicity, one between ~23.5 and ~23.8 Ma, and the other between ~22.4 and ~22.6 Ma (Fig. 5).

Cross-spectral analyses between the data records on the $CaCO_3$ tuned age model and eccentricity, indicate that $CaCO_3$ content, $\delta^{18}O$ and $\delta^{13}C$ are significantly coherent (99%) with eccentricity at the 405-ky, 125-ky and 95-ky eccentricity cycles (Fig. 5). Phase estimates of benthic $\delta^{18}O$ with respect to eccentricity indicates a lag of 20–35 ky at the 405 ky period, and 2–18 ky at the ~110 ky periodicity. The $\delta^{13}C$ record lags eccentricity by 19–38 ky at the 405-ky cycle, by 5–8 ky at the 125-ky cycle and by 8–10 ky at the 95-ky cycle (Fig. 5). $CaCO_3$ is roughly in-phase with eccentricity by 0-7 ky at the 405 ky cycle, 125-ky cycle and 95-ky cycle, which is not surprising, because it was used to obtain astronomically tuned ages. These phase relationships between $CaCO_3$ and eccentricity thus confirm that the in-phase tuning assumption was applied successfully.

4.3.2. Astronomical tuning using the benthic $\delta^{13}C$ record

An important consequence of the $CaCO_3$ tuned age model is that eccentricity-related variability within the benthic foraminiferal $\delta^{13}C$ record is not in-phase with eccentricity (Fig. 7b). On both the initial magnetostratigraphic age model and on the $CaCO_3$ tuned age model, the phase-lag, as identified in the filtered records, between the 405-ky-eccentricity cycle and the 405-ky cycle in $\delta^{13}C$ increases during the Early

Miocene (Figs. 6 and 7). The 405-ky eccentricity pacing of $\delta^{13}C$ is a consistent feature that characterizes the Cenozoic carbon cycle [*Holbourn et al*., 2004, 2013; *Littler et al*., 2014; *Pälike et al*., 2006a,b; *Liebrand et al*., 2016]. To date, no large changes in the phase-relationship of this cycle to eccentricity have been documented. An increased phase lag in the response of the 405-ky cycle to eccentricity, as is suggested by the $CaCO_3$ tuned age model, could provide further support for a large-scale reorganization of the carbon cycle across the OMT as has previously been suggested based on proxy studies [*Diester-Haas et al*., 2011, *Mawbey and Lear*, 2013]. Alternatively, the phase-lag of the 405-ky cycle in benthic $\delta^{13}C$ to eccentricity remains relatively small, which would indicate that the tuning assumptions underpinning the $CaCO_3$ tuned age model are flawed.

To distinguish between these two contrasting hypotheses, we generate another astronomically tuned age model. This time, we select the benthic $\delta^{13}C$ record as the tuning signal and assume that the 405-kyr and ~110-ky cycles in benthic $\delta^{13}C$ are continuously in phase with eccentricity across the OMT (Fig. 7d). Approximately five 405-ky cycles are identified in the benthic $\delta^{13}C$ record, which facilitate initial visual alignment to the same cycle in the eccentricity solution. Subsequently, we correlated the maxima and minima in the of the benthic $\delta^{13}C$ record, as identified in Gaussian filters of this data on the initial magnetostratigraphic age model (Fig. 7a), to those identified in the filtered component of the eccentricity solution (Fig. 7d).

The data records, on the benthic $\delta^{13}C$ tuned age model, span the interval between 22.1 and 24.2 Ma (i.e., 2.1 My duration), resulting in an average time step of 3.4 ky for the benthic stable isotope records. LRS range from 0.7–3.3 cm/ky, with an abrupt and short-lived increase across the OMT to ~1.7 cm/ky. On the $\delta^{13}C$ tuned age model, the $CaCO_3$ record remains in anti-phase with respect to ~110-ky eccentricity, but the benthic $\delta^{13}C$ tuning results in an alternative alignment $CaCO_3$ maxima to eccentricity minima that result in a ~110-ky shorter duration of the data records (Fig. 6 and 7). The evolutive analyses and power spectra are broadly consistent with the evolutive analyses from the $CaCO_3$ tuned age model, with dominant 405-ky cyclicity in all three datasets, an increase in spectral power at ~110-ky eccentricity cycles after the OMT and intermittent expression of higher frequency astronomical cycles. On the $\delta^{13}C$

tuned age model, all datasets exhibit a more significant response at the 95-ky short eccentricity cycle than the 125-ky short eccentricity cycle, in contrast to the $CaCO_3$ tuned age model. Significant power at the 41-ky obliquity periodicity is present in the late Oligocene, between ~ 23.3 and 23.8 Ma.

Cross-spectral analyses between data records on the $\delta^{13}C$ tuned age model and eccentricity (Fig. 5) indicate that $CaCO_3$, $\delta^{18}O$ and $\delta^{13}C$ are significantly coherent (99%) with eccentricity at the 405-, 125- and 95-ky eccentricity cycles. Phase estimates of $\delta^{18}O$ with respect to eccentricity (Fig. 5) shows lags of 1–9 ky at the 405-ky period and of 1–10 ky at the ~125 ky cycle. Benthic $\delta^{13}C$ lags eccentricity by 1–8 ky at the 405-ky periodicity and by 2–10 ky at the ~125-ky eccentricity cycle. At the 95-ky eccentricity cycle, $\delta^{13}C$ and $\delta^{18}O$ lead eccentricity by 1–9 ky. $CaCO_3$ leads eccentricity by 15–40 ky at the 405-ky cycle, by 0–14 ky at the ~125-ky cycle, and by 1–13 ky at the ~95-ky cycle.

5. Spreading rates

To independently test whether the $CaCO_3$ tuned ages or the benthic $\delta^{13}C$ tuned ages and their underlying phase-assumption, are most appropriate for tuning the deep marine Oligocene-Miocene records from Site U1334, we use independent ages based on plate pair spreading rates as a control age. When multiple plate pairs show simultaneous changes in spreading rate with the same ratio, e.g., all are faster by say 15% in a short time interval, this indicates errors in the timescale. We propose to use the age model that passes this test most successfully to provide ages for C6Bn.1n (o) to C6Cn.1r (o) and potentially revise those currently presented in the GTS2012.

Of the two astronomically tuned age models and GTS2012, the $CaCO_3$ tuned age model is most consistent with the least amount of changes in plate-pair spreading rates (Fig. 8). This suggests that a lithologic proxy record is the most suitable signal curve for Oligocene-Miocene records from the equatorial Pacific. It may also provide support for similar astronomical age calibration approaches that have been used for Middle Miocene [*Kochhann et al*., 2016] and Eocene-Oligocene [*Westerhold et al*., 2015] records from the equatorial Pacific Ocean, and for Oligocene-Miocene records from the South Atlantic Ocean [*Liebrand et al*., 2016]. Although these studies also used $CaCO_3$-controlled lithological proxy records for tuning to eccentricity, we note that these records show variable amounts of productivity versus dissolution as the main source of variance in the data.

On the $CaCO_3$ tuned age model, the Australia-Antarctica, Pacific-Nazca, and Pacific-Antarctic plate pairs are all very close to a constant spreading rate, at least prior to Chron C6Bn. The Juan de Fuca-Pacific plate-pair indicates a sudden decrease in spreading rate (145 to 105 mm/yr) at ~23 Ma, consistent with expectations [*Wilson*, 1988]. The implied synchronous changes for the Australia-Antarctica, Pacific-Nazca, and Pacific-Antarctic plate pairs in the $\delta^{13}C$ tuned age model, especially the faster spreading rates ~22.5-23.0 Ma implied by older ages for C6Bn, make this option less plausible. Differences between the $CaCO_3$ tuned age model for Site U1334 and GTS2012 are subtler. The longer duration of C6Cn.3n in the $CaCO_3$ tuned age model (106 vs. 62 kyr) eliminates a brief pulse of fast spreading implied by GTS2012, visible in Figure 8a as positive slopes in age-distance during that chron. Over longer intervals, $CaCO_3$ tuned ages remove a slight but synchronous rate slowdown that is also implied by GTS2012 and which starts at ~23.2 Ma.

The spreading rates computed using the $CaCO_3$ tuned age model suggest a duration for C6Cn.2n of 67 ky. This duration may be up to ~40 ky too short, as is suggested by the implied fast spreading during this chron (see the positive slopes in Figure 8b). Although our distance error bars indicate that this discrepancy is only marginally significant, it provides further support for an age of ~23.06 Ma for the Oligocene-Miocene boundary, broadly in agreement with independently tuned ages from Site 1264 [*Liebrand et al*., 2016]. This could indicate an uncertainty in the magnetostratigraphy at Site U1334, although this is unlikely as the C6Cn.2n reversal is clearly delineated in the Virtual Geomagnetic Pole (VGP) latitude signal [*Channell et al*., 2013]. In both the $CaCO_3$ content and $\delta^{13}C$ record, this short interval is difficult to align to the tuning target (Figs. 5 and 6), because $CaCO_3$ content values are high, with little variability and benthic $\delta^{13}C$ values corresponds to the marked shift towards higher values at the Oligocene-Miocene carbon maximum [*Hodell and Woodruff*, 1994]. The 83 kyr duration of C6Cn.2n from the $\delta^{13}C$ tuned age model is somewhat more consistent with spreading rates than the 67 kyr duration from the $CaCO_3$ tuned age model, and the 118 kyr duration in GTS2012 is even more consistent. If there is a problem with the tuning in both records for this chron, using constant spreading rates to interpolate from the adjacent $CaCO_3$ ages would imply reversal ages for the top and bottom of C6Cn.2n of ~22.95 and ~23.06 Ma. On significant difference the $CaCO_3$ tuned ages suggest is that the increase in spreading rates of the Juan de Fuca-Pacific plate-pair occurred approximately 200 ky later than those ages presented in the GTS2012 (i.e. during Chron C6Cn.2n. instead of C6Cn.3n, respectively; see Fig 8). Overall the spreading rates suggest that the $CaCO_3$ tuned age model is the preferred age model option.

6. Discussion

6.1. Age model evaluation

The final eccentricity tuned age models for the OMT time interval differ for two reasons. Firstly, there are 21 complete 110 ky cycles in the $\delta^{13}C$ tuned age model, and 22 in the $CaCO_3$ content record, making the $\delta^{13}C$ tuned age model ~1 eccentricity cycle shorter in duration. This is a direct result of the patterns observed in the 405 ky and ~110 ky cycles in the $CaCO_3$ and $\delta^{13}C$ datasets on the initial magnetostratigraphic age model. The tuned age models are consistent with each other across the positive $\delta^{18}O$ isotope excursion during the OMT, with the peak positive value in the $\delta^{18}O$ record, and the base of Chron C6Cn.2n (marking the Oligocene-Miocene boundary), occurring within 10 ky on both age models. They diverge at ~22.7 Ma, where the $CaCO_3$ content has an additional ~110 ky cycle on the initial magnetostratigraphic age model. Here, either the ~110 ky response at 22.7 Ma has not been recorded in the $\delta^{13}C$ record or there is a double peak in the $CaCO_3$ content. If we assign these contrasting ages to the selection of plate pair anomaly profiles, their spreading rates histories support the $CaCO_3$ tuned ages. In the depth domain, the existence of two distinct ~110-ky minima in the $\delta^{18}O$ record between 97.5 and 99 CCSF-A lends additional support to the $CaCO_3$ content age model.

6.2. Phase relationships

The second factor contributing to the difference between the age models is the different phase relations between $\delta^{13}C$ and eccentricity and $CaCO_3$ and eccentricity, which account for up to ~30 ky difference between the ages of maxima and minima in ~110 kyr cycles in the two records. One of the assumptions of our $CaCO_3$ content tuning is that it is more likely to be in-phase with eccentricity modulation of precession than the benthic $\delta^{18}O$ and $\delta^{13}C$ stable isotope records [*Pälike* et al., 2006a,b; *Liebrand et al*., 2011]. Variations in the $\delta^{13}C$ signal are generally considered to best reflect global ocean signals, but are thought to lag global climate by ~10% on all periodicities (Table 2) [*Billups et al*., 2004; *Pälike et al*., 2006a,b; *Liebrand et al*., 2016). The $CaCO_3$ signal, in contrast, most likely represents a more regional, ocean-basin wide response to insolation because it depends on regional carbonate productivity, dissolution and/or dilution. These processes affecting the $CaCO_3$ content of the sediment were probably more directly responsive to insolation forcing [*Hodell et al*., 2001]. The longer lag time of $\delta^{13}C$ with respect to eccentricity in comparison with $CaCO_3$ leads to older ages assigned to ~110 kyr maxima and minima in the $\delta^{13}C$ age model. This is particularly notable between 22.7 Ma and 24.2 Ma, when the age difference between the age models is accounted for only by the difference in phase. As the spreading rates support the $CaCO_3$ tuned ages, this implies that the long phase lag in the response of $\delta^{13}C$ to eccentricity results in less accurate tuned ages for Site U1334. This suggests that local/regional tuning signals produce more accurate age models in comparison with globally integrated isotope records, which are known to produce significant lags relative to eccentricity as a result of non-linear feedbacks [*Pälike et al*., 2006b, *Zeebe et al*., 2017].

6.3. Implications for the carbon cycle

Benthic foraminiferal $\delta^{13}C$ variations in the open ocean are typically interpreted to reflect the ratio between global organic and inorganic carbon burial [*Shackleton*, 1977; *Broecker*, 1982; *Diester-Haas et al*., 2013, *Mawbey and Lear*, 2013]. Astronomical forcing of organic carbon burial is typically expected in the precessional band because organic carbon burial, notably in the marine realm, depends on clay fluxes and thus hydrology (*Berner et al*., 1983). However, the residence time of carbon (~100 kyr) is so long (*Broecker and Peng*, 1982) that this energy is transferred into eccentricity bands (e.g., *Pälike et al*., 2006; *Ma et al*., 2011). Importantly, while the total marine carbon inventory is driven by ocean chemistry, the phase lag between eccentricity forcing and $\delta^{13}C$ should primarily be a function of the residence time of carbon (*Zeebe et al.*, 2017). Hypothetically, a change in total organic matter burial will only result in whole-ocean steady state when the $\delta^{13}C$ of buried carbon equals that of the input (through rivers). Because the burial fluxes are small compared to the total carbon inventory, a pronounced time lag between eccentricity forcing and $\delta^{13}C$ is expected (e.g., *Zeebe et al.*, 2017).

Interestingly, the $CaCO_3$ age model for Site U1334 implies that the phase lag between the 405 ky cycle in the $\delta^{13}C$ record and the eccentricity forcing increases across the OMT. A similar shift in phase is also present in the benthic foraminiferal $\delta^{13}C$ record from 1264 [*Liebrand et al.*, 2011; *Liebrand et al.*, 2016]. In theory (*Zeebe et al.*, 2017), an increase in the phase lag suggests an increase in the residence time oceanic carbon, either through a rise in the total carbon inventory or a drop in the supply and burial of carbon. The lengthening of the phase lag of the 405 ky cycle coincides with a large shift in the benthic foraminiferal $\delta^{13}C$ record across the OMT to more positive values, evidencing a structural relative increase in the supply of ^{13}C-depleted or drop in the burial of ^{13}C-enriched carbon. Reliable reconstructions of CO_2 are rare across the OMT (www.p-co2.org) and the OMT does not seem associated with a large change in the depth of the Pacific calcite compensation depth (*Pälike et al*., 2012). Therefore, additional constraints on atmospheric CO_2 concentrations and burial fluxes are required to speculate on the mechanisms associated with the increased phase lag.

7. Conclusions

We explore the application of $CaCO_3$ content and benthic foraminiferal $\delta^{13}C$ records as tuning signals for the OMT record at Site U1334 in the eastern equatorial Pacific. These two tunings highlight the importance of carefully considering the implications of tuning choices and assumptions when creating astronomical age models. Spreading rate histories provide independent evidence for the astronomically tuned age models, and are generally in best agreement with the $CaCO_3$ tuned age model. This suggests that lithological signals respond more directly to insolation forcing than stable isotope signals, for which we find support for a delayed respond to astronomical climate forcing. The $CaCO_3$ based age model thus provides a valuable method to better understand the (lagged) response in benthic foraminiferal $\delta^{18}O$ and $\delta^{13}C$, which are widely used and reproducible proxies for the global climate/cryosphere system and (marine) carbon cycle. One important implication of the $CaCO_3$ age model is that 405 ky cycle in benthic $\delta^{13}C$ shows a distinct phase lag with respect to orbital eccentricity. Lastly, the $CaCO_3$ age model for Site U1334 provides astronomically calibrated ages for C6AAr.3r to C6Cn.1r, which in GTS2012 are not presently astronomically calibrated. The polarity chron ages from the $CaCO_3$ tuned ages are generally older by approximately 60 ky on average than those presented in the GTS2012. We suggest that these updated early Miocene ages are incorporated in the next version of the GTS.

Acknowledgements

This research used samples provided by the Integrated Ocean Drilling Program (IODP), collected by the staff, crew and scientists of IODP Expedition 320/321. We thank Dominika Kasjanuk, Arnold van Dijk, Maxim Krasnoperov and Jan Drenth for laboratory assistance. Linda Hinnov kindly provided her evolutive analysis MATLAB script. This research was supported by PalaeoClimate.Science (DL), NWO grant 865.10.001 (L.J.L), ERC grant 259627 (A.S.), NERC grant NE/G014817 (B.S.W.), and a Marie Curie Career Integration Grant "ERAS". All data are available online (www.pangaea.de). *(NB. Data will be uploaded after acceptance for publication and DOI link will be provided).*

Figure Captions

Figure 1. Locations of ODP and IODP drill sites discussed in this study. Location of IODP Site U1334 with reference to ODP Sites 1264, 1218, 926, 929 and 1090.

Figure 2. Calibration between the shipboard Magnetic Susceptibility record and shipboard coulometric $CaCO_3$ measurements to obtain a record of $CaCO_3$ estimates (wt%). (a) The Magnetic susceptibility and $CaCO_3$ content records. **(b)** The relationship between coulometric $CaCO_3$ measurements and discrete sample magnetic susceptibility was calculated using ordinary least squares linear regression, and yielded an r^2 value of 0.79.

Figure 3. Site U1334 datasets, evolutive spectra and power spectra against depth. (a) Magnetostratigraphy for Site U1334 (*Channell et al.*, 2013). **(b)** The $CaCO_3$ content record. **(c)** The benthic foraminiferal $\delta^{18}O$ record. **(d)** The benthic foraminiferal $\delta^{13}C$ record. **(e)** Evolutive and power spectra of the $CaCO_3$ content record. **(f)** Evolutive and power spectra of the benthic foraminiferal $\delta^{18}O$ record. **(g)**

Evolutive and power spectra of the benthic foraminiferal $\delta^{13}C$ record. All data plotted against the latest available splice (*Westerhold et al.*, 2012)

Figure 4. Depth versus age relationships for the different age models for Site U1334. Magnetochron ages are based on GTS2012 [*Vandenberghe et al.*, 2012; *Hilgen et al.*, 2012], the initial age model, the $CaCO_3$ content age model and the $\delta^{13}C$ age model. Magnetochrons are plotted as colored circles, and the lines represent a third order polynomial fit.

Figure 5. **Implication of age models on time series analysis. (a-c)** $CaCO_3$ on the initial, $CaCO_3$ tuned, and the $\delta^{13}C$ tuned age model, respectively. **(d-f)** As in (a-c) but for benthic foraminiferal $\delta^{18}O$. **(g-i)** As in (a-c) but for benthic foraminiferal $\delta^{13}C$. Prior to analysis, the $CaCO_3$ data are resampled at a time step of 2 ky, the benthic foraminiferal data are resampled at a time step of 4 ky. For all records, periodicities larger than 600 ky are notch-filtered out. Coherence and phase estimates are between eccentricity La2011 solution and benthic isotope datasets. The significance level represented by the red line for the coherence plots is 99%. For the phase estimates between the benthic foraminiferal series and eccentricity, eccentricity was multiplied by −1.

Figure 6. Site U1334 $CaCO_3$ versus age. (a) The $CaCO_3$ dataset and Gaussian filters plotted on **(a)** the magnetostratigraphic age model, **(b)** the $\delta^{13}C$ tuned age model, and **(c)** the $CaCO_3$ tuned age model. **(d)** Earth's orbital eccentricity solution is plotted in grey [*Laskar et al*., 2010, *Laskar et al*., 2011]. Tie points are represented by red dots and dashed lines. Gaussian filters were calculated in AnalySeries [*Palliard et al*., 1996] with the following settings: 405 ky *– f : 2.5 bw 0.8,* ~110 ky *– f : 10, bw : 3.* **(e)** Sedimentation rates are calculated using the $CaCO_3$ tuned age model.

Figure 7. **Site U1334 $\delta^{13}C$ versus.** The $\delta^{13}C$ dataset and Gaussian filters plotted on **(a)** the magnetostratigraphic age model, **(b)** the $CaCO_3$ tuned age model, and **(c)** the $\delta^{13}C$ tuned age model. **(d)** Earth's orbital eccentricity solution is plotted in grey [*Laskar et al*., 2010, *Laskar et al*., 2011]. Tie points are represented by red dots and dashed lines. Gaussian filters were calculated in AnalySeries [*Palliard et al*., 1996]

with the following settings: 405 ky – *f : 2.5 bw 0.8,* ~110 ky – *f : 10, bw : 3.* **(e)** Sedimentation rates are calculated using the $\delta^{13}C$ age model.

Figure 8. **Plate-pair spreading rates based on different age models.** Reduced-distance plots for the labeled plate pairs implied by **(a)** the GTS2012, **(b)** the $CaCO_3$ tuned age model and **(c)** the $\delta^{13}C$ tuned age model. Reduced distance is the full spreading distance (D) minus the age (A) times the labeled spreading rate (R, see y-axes). Distance scale is plotted inversely with spreading rate so that for true constant spreading rate, age errors will cause uniform vertical departures from a straight line. Error bars are 95% confidence. The $CaCO_3$ based age model **(b)** gives the simplest spreading rate history.

Table 1. Comparison of magnetostratigraphic reversal ages. Chron boundary ages across the Oligocene Miocene Transition from the published literature and this study. Age differences are presented on the right hand side.

Table 2. Comparison of tuning methods and phase relationships. List of astronomically dated Oligocene-Miocene spanning record. Tuning signal and target curves, and phase relationships to the target curves are compared.

References

Barckhausen, U., C. R. Ranero, S. C. Cande, M. Engels and W. Weinrebe (2008), Birth of an intraoceanic spreading center. *Geology*, *36*(10), 767-770.

Beddow, H. M., D. Liebrand, A. Sluijs, B. S. Wade, and L. J. Lourens (2016), Global change across the Oligocene-Miocene transition: High-resolution stable isotope records from IODP Site U1334 (equatorial Pacific Ocean), *Paleoceanography, 31, doi:10.1002/2015PA002820.*

Berner, R. A., A. C. Lasaga, and R. M. Garrels (1983), The carbonate-silicate geochemical cycle and its effect on atmospheric carbon dioxide over the past 100 million years. *American Journal of Science, 283,* 641–683, doi: 10.2475/ajs.283.7.641.

Billups, K., H. Pälike, J. E. T. Channell, J. C. Zachos, and N. J. Shackleton (2004), Astronomic calibration of the late Oligocene through early Miocene geomagnetic polarity time scale, *Earth Planet. Sci. Lett*., *224*, 33–44, doi:10.1016/j.epsl.2004.05.004.

Broecker, W. S. (1982), Glacial to interglacial changes in ocean chemistry, *Progress in Oceanography*, 11, 2, 151-197.

Broecker, W. S., T-H Peng (1982), Tracers in the Sea, Lamont-Doherty Geological Observatory, Columbia University.

Cande, S. C., and D. V. Kent (1992), A new geomagnetic polarity time scale for the Late Cretaceous and Cenozoic, *J. Geophys. Res.*, *97*(B10), 13917-13951.

Cande, S. C., and J. M. Stock (2004), Pacific-Antarctic-Australia motion and the formation of the Macquarie plate, *J. Geophys. Int.*, 157, 399-414.

Channel, J .E. T., C. Ohneiser, Y. Yamamoto, and M.S. Kesler (2013), Oligocene-Miocene magnetic stratigraphy carried by biogenic magnetite at sites U1334 and U1335 (equatorial Pacific ocean) *Geochemistry, Geophysics, Geosystems, 14*(2) pp1525-2027doi:10.1029/2012GC004429.

Croon, M. B., S. C. Cande, and J. M. Stock (2008), Revised Pacific-Antarctic plate motions and geophysics of the Menard Fracture Zone: *Geochemistry, Geophysics, Geosystems*, v. 9, Q07001, doi:10.1029/2008GC002019.

DeConto, R.M., S. Galeotti, M. Pagani, D. Tracy, K. Schaefer, T. Zhang, D. Pollard, and J.D. Beerling, (2012). Past extreme warming events linked to massive carbon release from thawing permafrost. *Nature*, *484*(7392), p.87.

Diester-Haass, L., K. Billups, and K. Emeis (2011), Enhanced paleoproductivity across the Oligocene/Miocene boundary as evidenced by benthic foraminiferal accumulation rates. *Palaeogeography, Palaeoclimatology, Palaeoecology* 302, 464 - 473 doi:10.1016/j.palaeo.2011.02.006.

Diester-Haass, L., K. Billups, I. Jacquemin, K.C. Emeis, V. Lefebvre and L. François, (2013). Paleoproductivity during the middle Miocene carbon isotope events: A data-model approach. *Paleoceanography*, *28*(2), 334-346.

Gradstein, F. M., J. G. Ogg, M. D. Schmitz and G. M. Ogg (2012), *The geologic time scale 2012*.

Herbert, T. D (1994), Reading orbital signals distorted by sedimentation: models and examples. *Orbital forcing and cyclic sequences*, 483-507.

Hilgen, F. J., L. J. Lourens, and J. A. Van Dam (2012), The Neogene Period. *The geologic time scale*, *2*, 923-978.

Hodell, D. A., and F. Woodruff (1994), Variations in the strontium isotopic ratio of seawater during the Miocene: Stratigraphic and geochemical implications. *Paleoceanography* **9**, 405-426.

Hodell, D.A., C.D. Charles and F.J. Sierro (2001), Late Pleistocene evolution of the ocean's carbonate system. *Earth and Planetary Science Letters*, *192*(2), pp.109-124.

Holbourn, A., W. Kuhnt, J. T. Simo and Q. Li (2004), Middle Miocene isotope stratigraphy and paleoceanographic evolution of the northwest and southwest Australian margins (Wombat Plateau and Great Australian Bight). *Palaeogeography, Palaeoclimatology, Palaeoecology*, *208*(1), 1-22.

Holbourn, A., W. Kuhnt, S. Clemens, W. Prell, and N. Andersen (2013), Middle to late Miocene stepwise climate cooling: Evidence from a high-resolution deep-water isotope curve spanning 8 million years, *Paleoceanography, 28*, doi:10.1002/2013PA002538.

Hüsing, S. K., F. J. Hilgen, H. Abdul Aziz, and W. Krijgsman (2007), Completing the Neogene geological time scale between 8.5 and 12.5 Ma, *Earth and Planetary Science Letters*, *253*, 340-358.

King, T. (1996). Quantifying nonlinearity and geometry in time series of climate. *Quaternary Science Reviews*, *15*(4), 247-266.

Krijgsman, W., F. J. Hilgen, I. Raffi, F. J. Sierro and D. S Wilson (1999), Chronology, causes and progression of the Messinian salinity crisis. *Nature*, *400*(6745), 652-655.

Kochhann, K. G., Holbourn, A., Kuhnt, W., Channell, J. E., Lyle, M., Shackford, J. K., Andersen, N. (2016). Eccentricity pacing of eastern equatorial Pacific carbonate dissolution cycles during the Miocene Climatic Optimum. *Paleoceanography*, *31*(9), 1176-1192.

Laskar, J., P. Robutel, F. Joutel, M. Gastineau, A. C. M Correia, and B. Levrard (2004), A long-term numerical solution for the insolation quantities of the Earth. *Astronomy & Astrophysics*, *428*(1), 261-285.

Laskar, J., A. Fienga, M. Gastineau, and H. Manche (2011a), La2010: A new orbital solution for the long term motion of the Earth, *Astronomy and Astrophysics*, *532*(A89).

Laskar, J., M. Gastineau, J.-B. Delisle, A. Farrés, and A. Fienga (2011b), Strong chaos induced by close encounters with Ceres and Vesta, *Astronomy and Astrophysics*, *532*(L4), 1-4.

Liebrand, D., L. Lourens, D. A. Hodell, B de. Boer, R. S. W. van der Wal, and H. Pälike (2011), Antarctic ice sheet and oceanographic response to eccentricity forcing in the early Miocene. *Climates of the past, 7*, pp 869 - 880.

Clim. Past Discuss., https://doi.org/10.5194/cp-2017-135
Manuscript under review for journal Clim. Past
Discussion started: 25 October 2017

Liebrand, D., H. M. Beddow, L. J. Lourens, H. Pälike, I. Raffi, S. M. Bohaty, F. J. Hilgen, Mischa J. M. Saes., P.A. Wilson, A. E. van Dijk, D. A. Hodell, D. Kroon., C. E. Huck and S. J. Batenburg (2016). Cyclostratigraphy and eccentricity tuning of the early Oligocene through early Miocene (30.1-17.1 Ma): Cibicides mundulus stable oxygen and carbon isotope records from Walvis Ridge Site 1264. *Earth and Planetary Science Letters, 450*, 392-405.

Liebrand, D., et al. (2017), Evolution of the early Antarctic ice ages, *Proc. Natl. Acad. Sci. U. S. A.*, 114(15), 3867–3872.

Littler, K., U. Röhl, T. Westerhold, and J.C. Zachos (2014). A high-resolution benthic stable-isotope record for the South Atlantic: Implications for orbital-scale changes in Late Paleocene–Early Eocene climate and carbon cycling. *Earth and Planetary Science Letters*, *401*, 18-30.

Lonsdale, P., (2005), Creation of the Cocos and Nazca plates by fission of the Farallon plate: *Tectonophysics*, v. 404, p. 237–264, doi: 10.1016/ j.tecto.2005.05.011.

Lourens, L. J., F. J. Hilgen, N. J. Shackleton, J. Laskar and D. Wilson (2004),'Chapter 21: The Neogene Period'. In: Gradstein, F., Ogg, J. and Smith,A., (eds).,*A Geologic Time Scale 2004*, Cambridge University Press, Cambridge, pp. 409-440.

Ma, W., J. Tian, Q. Li, and P. Wang (2011), Simulation of long eccentricity (400-kyr) cycle in ocean carbon reservoir during Miocene Climate Optimum: Weathering and nutrient response to orbital change, *Geophys. Res. Lett., 38*, L10701, doi:10.1029/2011GL047680.

Paillard, D., L. Labeyrie, and P. Yiou (1996), Macintosh program performs time‐series analysis, *Eos Trans. AGU*, *77*, 379, doi:10.1029/96EO00259.

Pälike, H., J. Frazier, and J.C. Zachos (2006a), Extended orbitally forced palaeoclimatic records from the equatorial Atlantic Ceara Rise. *Quaternary Science Reviews,* 25, 3138–3149.

Pälike, H., R. N. Norris, J. Herrle, P. A. Wilson, H. K. Coxall, C. H. Lear, N. J. Shackleton, A. K. Tripati, and B. S. Wade (2006b), The heartbeat of the Oligocene climate system, *Science, 314*, 1894–1898, doi:10.1126/ science.1133822.

Pälike, H., M. W. Lyle, H. Nishi, I. Raffi, K. Gamage, A. Klaus and the Expedition 320/321 Scientists (2010), *Proceedings of the Integrated Ocean Drilling Program*, Volume 320/321. Tokyo (Integrated Ocean Drilling Program Management International, Inc.).

Pälike, H., M. W. Lyle, H. Nishi, I. Raffi, A. Ridgewell, K. Gamage, et al (2012), A Cenozoic record of the equatorial Pacific carbonate compensation depth, *Nature*, *488*(7413), 609-614.

Shackleton, N . J. (1977), Carbon-13 in Uvigerina: Tropical rain forest history and the equatorial Pacific carbonate dissolution cycles, in *The Fate of Fossil Fuel* CO_2 *in the Oceans*, edited by N.R. Andersen and A. Malahoff, 401-427, Plenum, New York,

Shackleton, N. J., S. J. Crowhurst, G. P. Weedon, and J. Laskar (1999), Astronomical Calibration of Oligocene-Miocene Time, *Philosophical Transactions: Mathematical, Physical and Engineering Sciences*, *357*(1757), 1907-1929.

Shackleton, N.J., M. A. Hall, I. Raffi, L. Tauxe, and J. C. Zachos (2000), Astronomical calibration age for the Oligocene/Miocene boundary. *Geology 28* (5), 447–450.

Vandenberghe, N., F. J. Hilgen, and R. P. Speijer (2012), The paleogene period. *The geologic time scale*, *2012*, 855-921.

Westerhold, T., et al. (2012a), Revised composite depth scales and integration of IODP Sites U1331–U1334 and ODP Sites 1218–1220, in *Proceedings of the Integrated Ocean Drilling Program*, vol. 320/321, edited by H. Pälike et al., Integ. Ocean Drill. Progr. Manage. Int., College Station, Tex.

Westerhold, T., U. Röhl and J. Laskar (2012b), Time scale controversy: Accurate orbital calibration of the early Paleogene. *Geochemistry, Geophysics, Geosystems*, *13*(6).

Westerhold, T., Röhl, U., Frederichs, T., Agnini, C., Raffi, I., Zachos, J. C., and Wilkens, R. H.: Astronomical Calibration of the Ypresian Time Scale: Implications for Seafloor Spreading Rates and the Chaotic Behaviour of the Solar System?, Clim. Past Discuss., doi:10.5194/cp-2017-15, in review, 2017.

Wilson, D. S (1988). Tectonic history of the Juan de Fuca ridge over the last 40 million years. *Journal of Geophysical Research: Solid Earth (1978–2012)*, *93*(B10), 11863-11876.

Wilson, D. S. (1993), Confirmation of the astronomical calibration of the magnetic polarity time scale from rates of sea-floor spreading, *Nature, 364*, 788-790.

Zachos, J. C., N. J. Shackleton, J. S. Revenaugh, H. Pälike, and B. P. Flower (2001), Climate response to orbital forcing across the Oligocene – Miocene boundary, *Science* 292, 274– 278.

Zeebe, R. E., T. Westerhold, K. Littler, J. C. Zachos (2017), Orbital forcing of the Paleocene and Eocene carbon cycle, *Paleoceanography, 32,* 440–465, doi:10.1002/2016PA003054.

Zeeden, C., F. J. Hilgen, S. K. Hüsing, and L. J. Lourens (2014), The Miocene astronomical time scale 9–12 Ma: new constraints on tidal dissipation and their implications for paleoclimatic investigations. *Paleoceanography*, *29*(4), 296-307.

Clim. Past Discuss., https://doi.org/10.5194/cp-2017-135
Manuscript under review for journal Clim. Past
Discussion started: 25 October 2017

Climate of the Past Discussions
Open Access

Figure 1

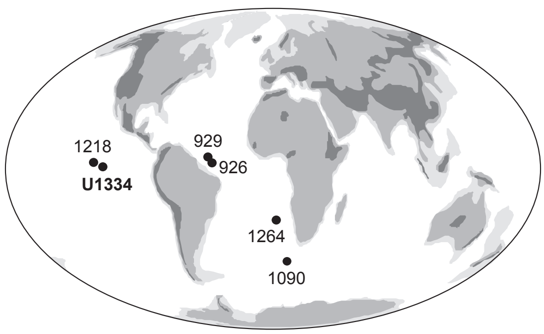

Clim. Past Discuss., https://doi.org/10.5194/cp-2017-135
Manuscript under review for journal Clim. Past
Discussion started: 25 October 2017

Climate of the Past Discussions

Figure 2

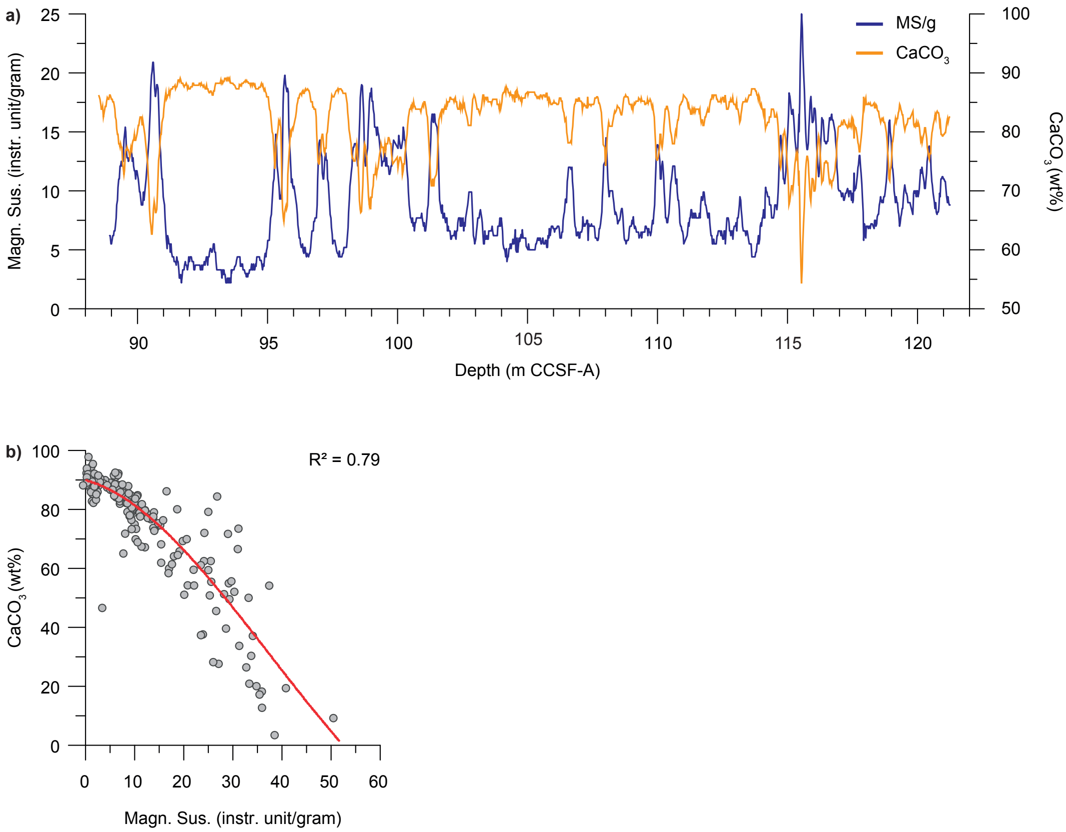

Clim. Past Discuss., https://doi.org/10.5194/cp-2017-135
Manuscript under review for journal Clim. Past
Discussion started: 25 October 2017

Climate of the Past Discussions
Open Access
EGU

Figure 3

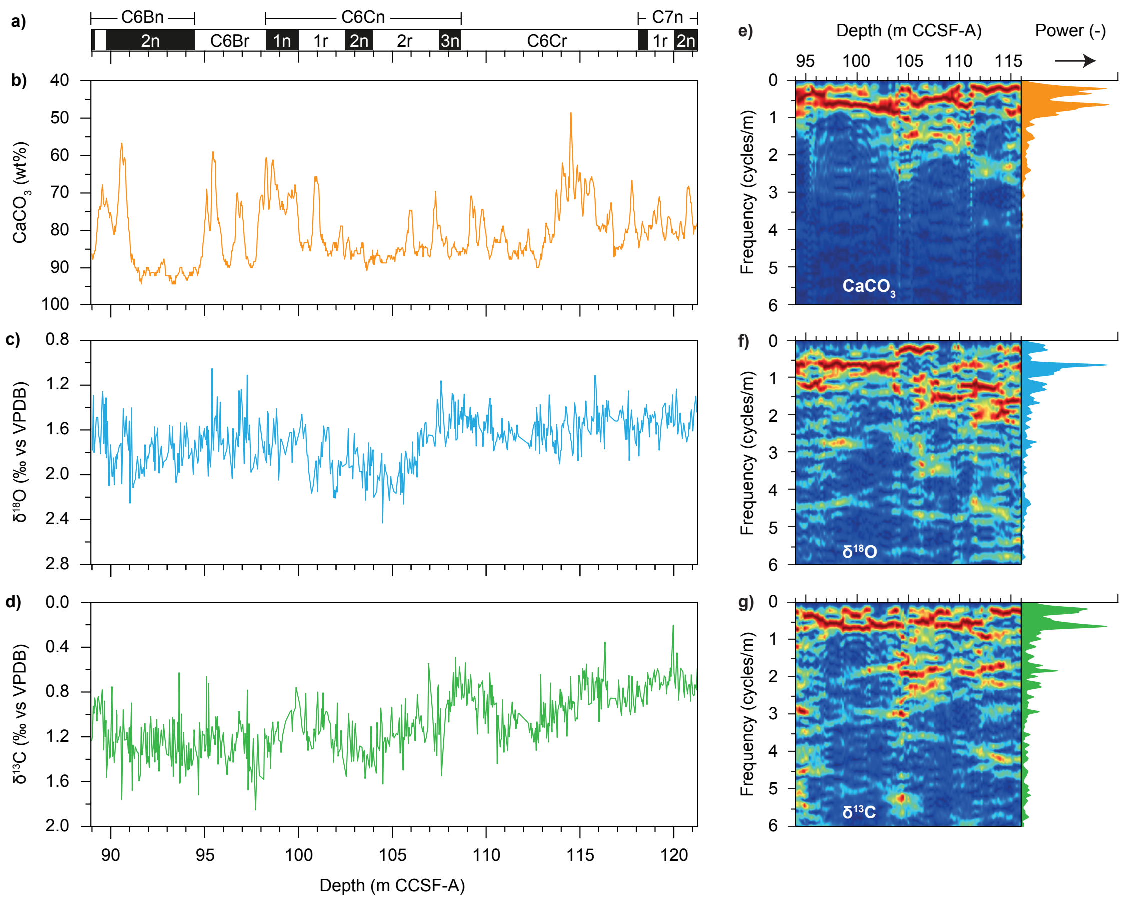

Clim. Past Discuss., https://doi.org/10.5194/cp-2017-135
Manuscript under review for journal Clim. Past
Discussion started: 25 October 2017

Climate of the Past Discussions
Open Access

Figure 4

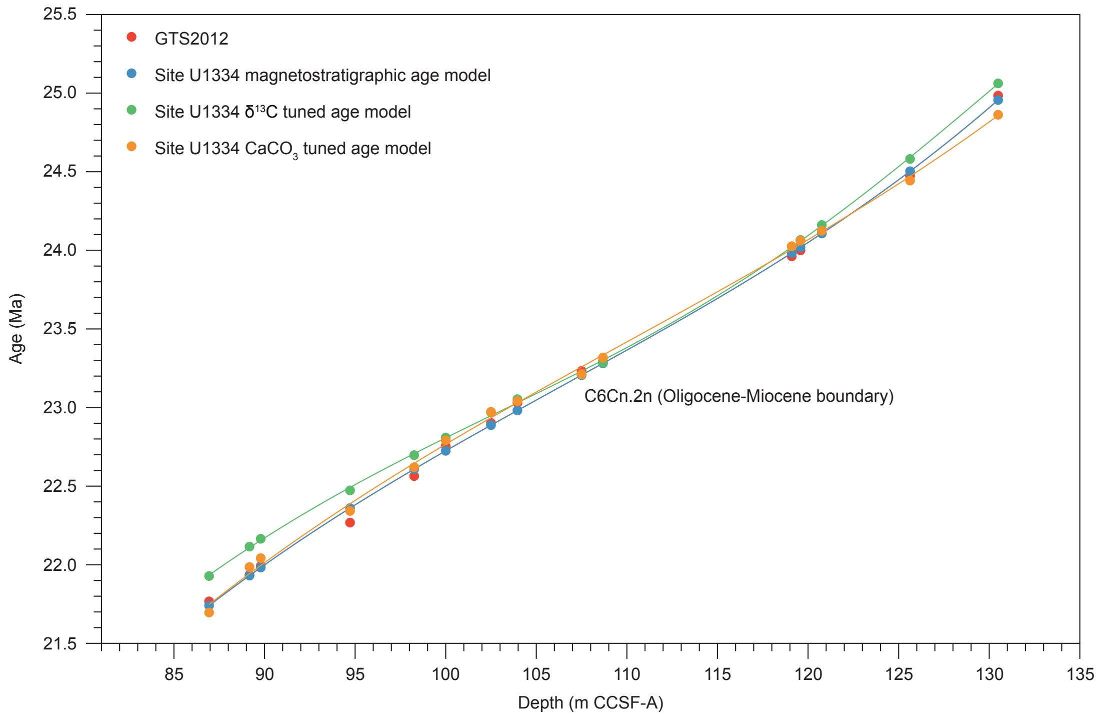

Clim. Past Discuss., https://doi.org/10.5194/cp-2017-135
Manuscript under review for journal Clim. Past
Discussion started: 25 October 2017

Figure 5

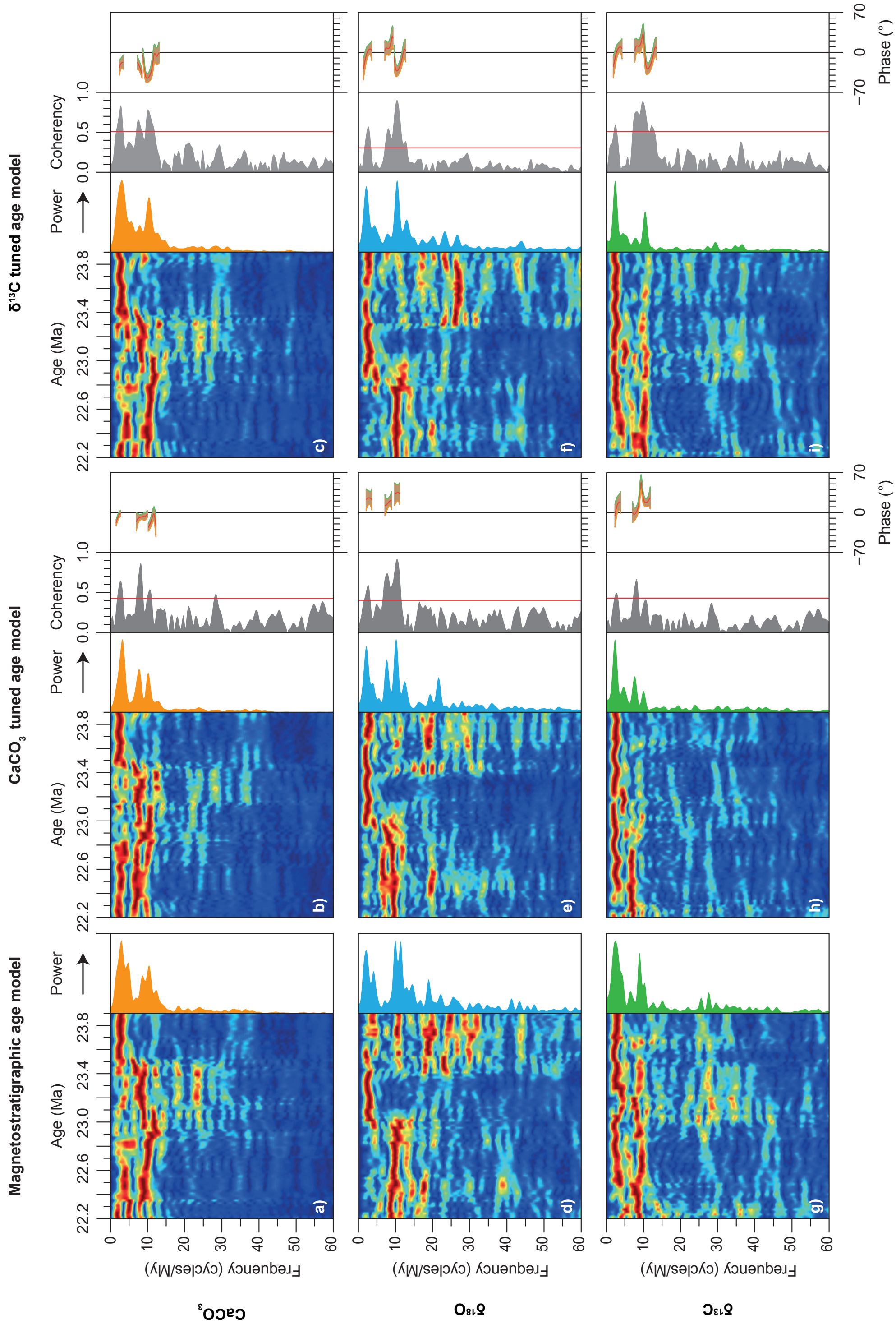

Figure 6

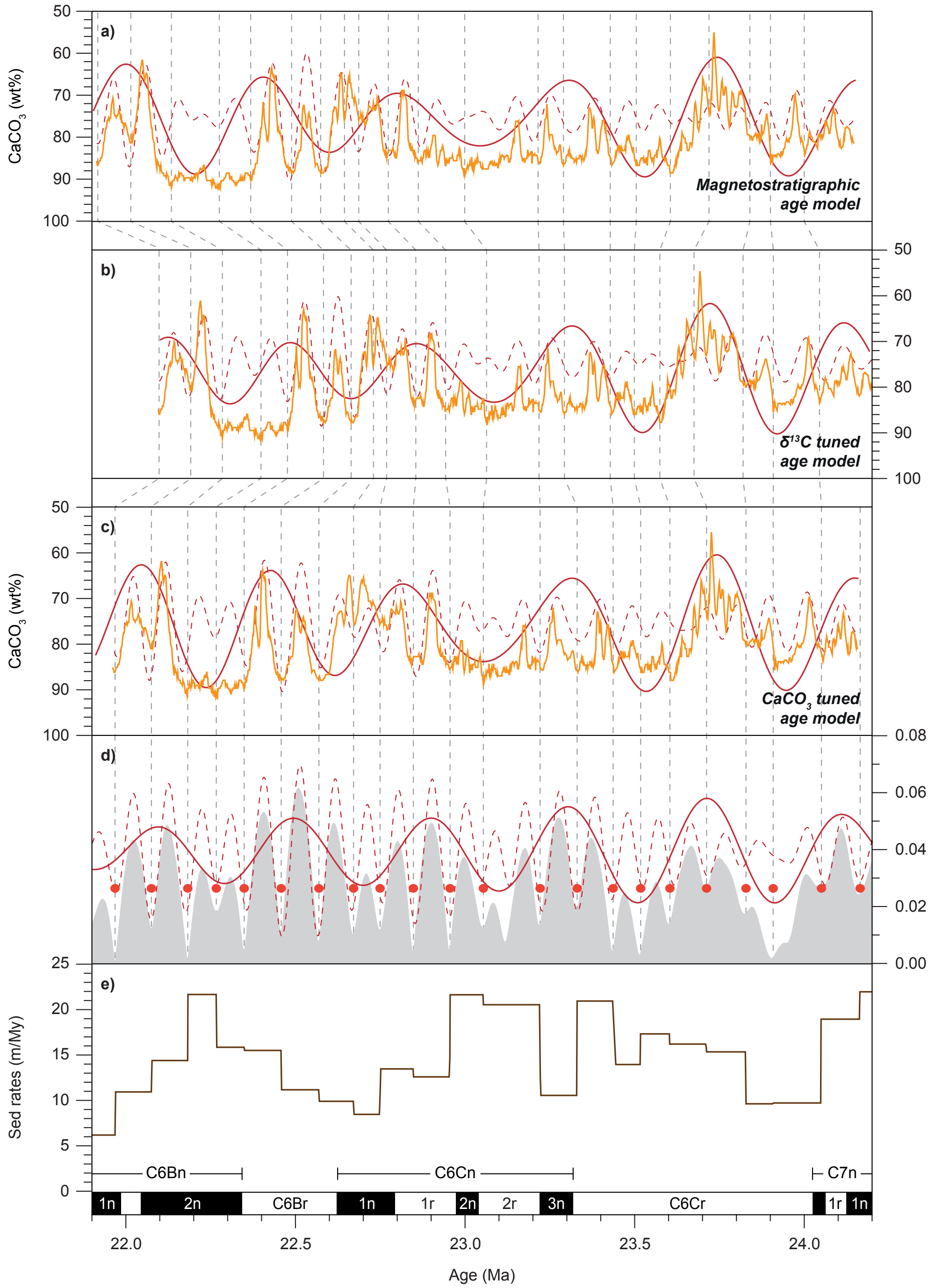
a)
b)
c)
d)
e)
CaCO$_3$ (wt%)
Magnetostratigraphic age model
δ^{13}C tuned age model
CaCO$_3$ tuned age model
Eccentricity (-)
Sed rates (m/My)
C6Bn
C6Cn
C7n
1n
2n
C6Br
1r
2r
3n
C6Cr
Age (Ma)

Clim. Past Discuss., https://doi.org/10.5194/cp-2017-135
Manuscript under review for journal Clim. Past
Discussion started: 25 October 2017

Climate of the Past Discussions
Open Access

Figure 7

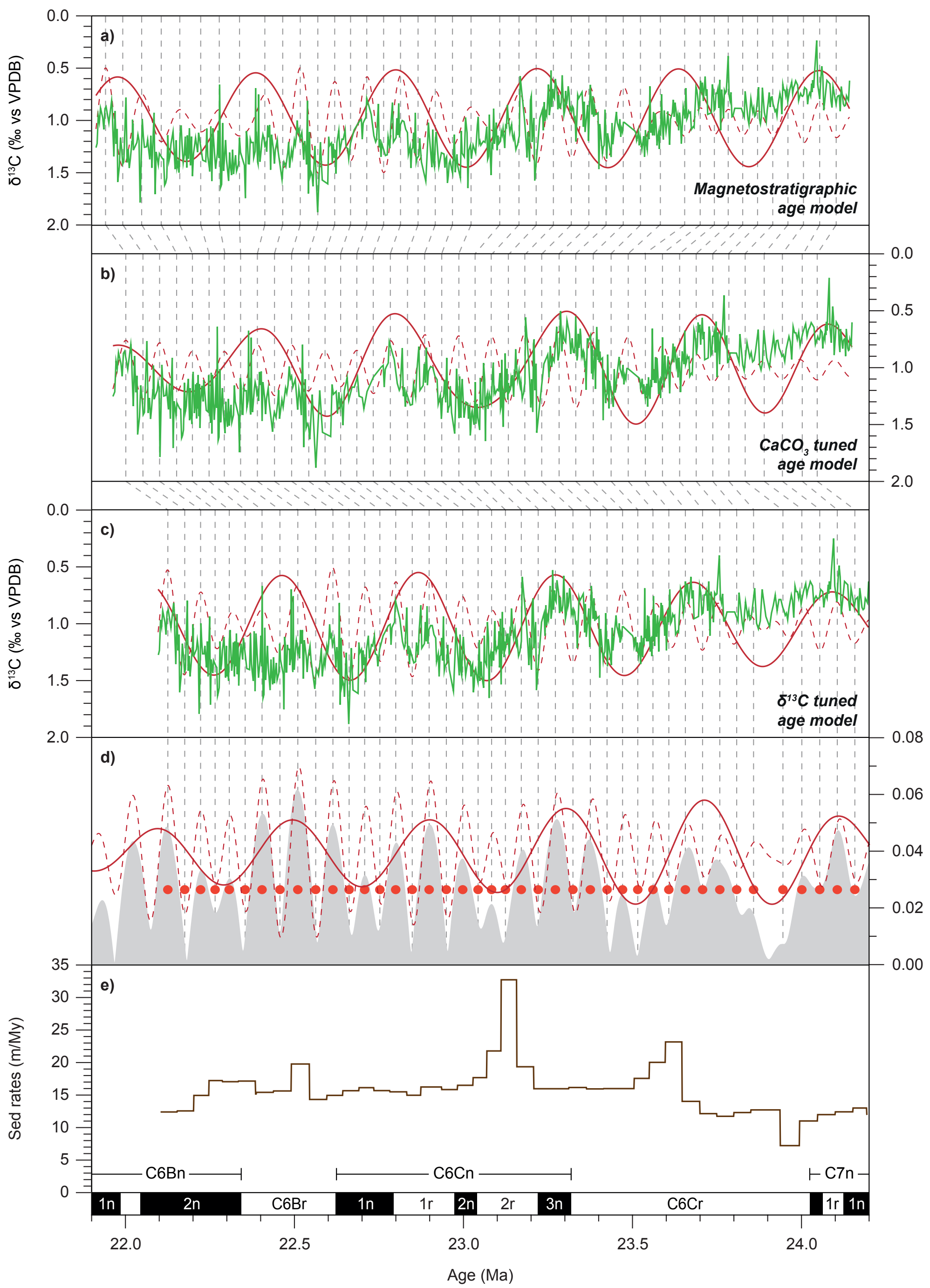

Clim. Past Discuss., https://doi.org/10.5194/cp-2017-135
Manuscript under review for journal Clim. Past
Discussion started: 25 October 2017

Climate of the Past Discussions
Open Access
EGU

Figure 8

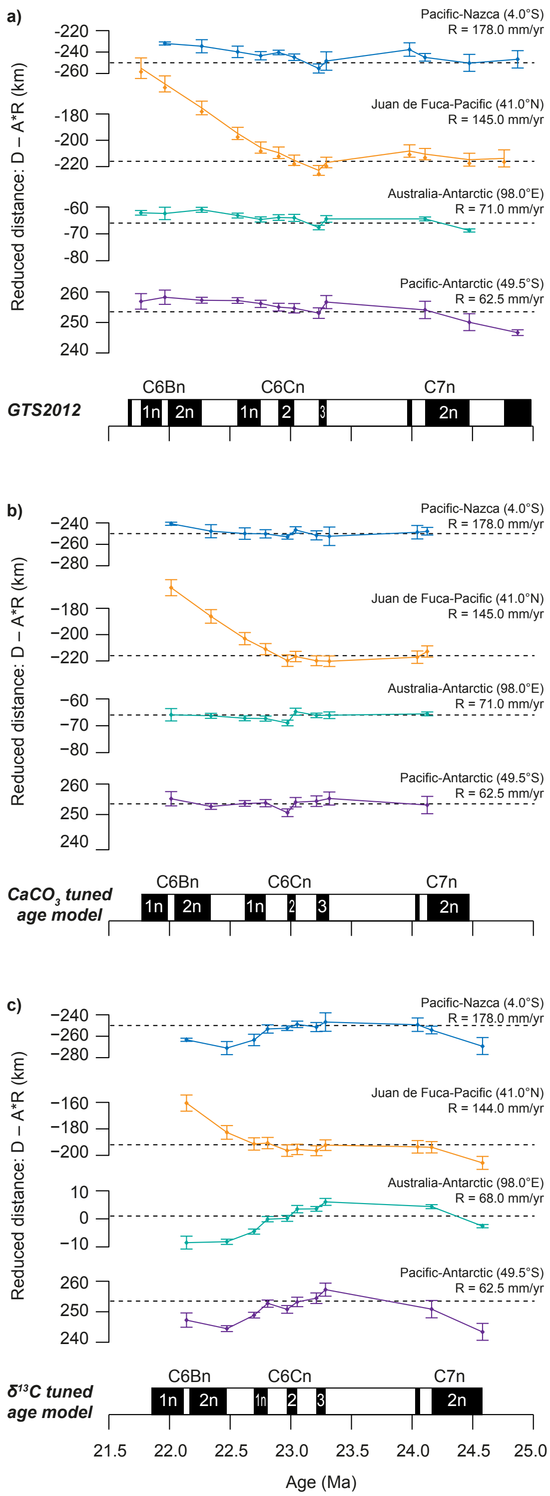

Table 1

Chron (old end)	**CCSF-A (m) [*Channell et al.*, 2013]**	**GTS2004 (Ma) [*Lourens et al, 2004]***	**GTS2012 (Ma) [*Hilgen et al.*, 2012]**	**Onset (Ma) *Billups et al,* 2004**	**Onset (Ma) *Palike et al,* 2006**	**Onset (Ma) $CaCO_3$ based astronomical tuning**	**Onset (Ma) $\delta^{13}C$ based astronomical tuning**	**Difference Between GTS2012 and *Billups et al.*, 2004 (Myr)**	**Difference Between GTS2012 and *Pälike et al.*, 2006 (Myr)**	**Difference Between GTS2012 and $CaCO_3$ based tuning (Myr)**	**Difference Between GTS2012 and $\delta^{13}C$ based tuning (Myr)**
C6Bn.1n	89.17	21.936	21.936	21.991	21.998	21.985	22.115	-0.055	-0.062	-0.049	-0.179
C6Bn.1r	89.79	21.992	21.992	22.034	22.062	22.042	22.165	-0.042	-0.070	-0.050	-0.173
C6Bn.2n	94.72	22.268	22.268	22.291	22.299	22.342	22.473	-0.023	-0.031	-0.074	-0.205
C6Br	98.26	22.564	22.564	22.593	22.588	22.621	22.697	-0.029	-0.024	-0.057	-0.133
C6Cn.1n	100.00	22.754	22.754	22.772	22.685	22.792	22.809	-0.018	0.069	-0.038	-0.055
C6Cn.1r	102.50	22.902	22.902	22.931	22.854	22.973	22.970	-0.029	0.048	-0.071	-0.068
C6Cn.2n	103.96	23.030	23.030	23.033	23.026	23.040	23.053	-0.003	0.004	-0.01	-0.023
C6Cn.2r	107.50	23.249	23.233	23.237	23.278	23.212	23.211	-0.004	-0.045	0.021	0.022
C6Cn.3n	108.68	23.375	23.295	23.299	23.340	23.318	23.286	-0.0026	-0.045	-0.023	0.009
C6Cr	119.10	24.044	23.962	23.988	24.022	24.025	24.026	-0.013	-0.060	-0.063	-0.064
C7n.1n	119.58	24.102	24.000	24.013	24.062	24.061	24.066	-0.029	-0.038	-0.061	-0.066
C7n.1r	120.76	24.163	24.109	24.138	24.147	24.124	24.161			-0.015	-0.052

Table 2

Site	Tuning signal	Tuning target	Lead/lag 405 kyr $\delta^{13}C$	Lead/lag ~110 kyr $\delta^{13}C$	Lead/lag ~405 kyr $\delta^{18}O$	Lead/lag ~110 kyr $\delta^{18}O$	Lead/lag ~405 kyr $CaCO_3$ est (%)	Lead/lag ~110 kyr $CaCO_3$ est (%)
Site U1334 (This study)	$CaCO_3$ est. %	Eccentricity	Lag ~30 kyrs	Lag ~10 kyrs	Lag ~25-30 kyrs	Lag ~10 kyrs	In phase	In phase
Site U1334 (This study)	Carbon isotopes	Eccentricity	In phase	Lag ~10 kyrs at 125 kyr, In phase at 96 kyr	In phase	Lag ~10 kyrs	Leads ~20 kyrs	Leads ~10 kyrs
Site 1090 (*Billups et al.*, 2004)	Oxygen isotopes	ETP	Lag ~20 -30 kyrs	Lag ~20 -30 kyrs	In phase	In phase at 125 kyr, ~10 kyr lag at 96 kyr	-	-
Site 926 (*Palike et al.*, 2006a)	Combination of magnetic susceptibility and colour reflectance (SusRef)	ETP	Lag ~35 kyrs	Lag ~30 kyrs	Lag ~ 10 kyrs	Lag ~20 kyrs	-	-
Site 1218 (*Palike et al.*, 2006b)	Carbon isotopes	ETP	Lag ~30 kyrs	In phase	Lag ~10 kyrs	In phase	-	-
Site 1264 (*Liebrand et al.*, 2016)	$CaCO_3$ est. (%)	Eccentricity	Lag ~36 kyrs	Lag ~12 kyrs	Lead ~14 kyrs	Lag ~12 kyrs	Unstable phase	In phase